PLOS ONE

RESEARCH ARTICLE

Novel magnetic multicore nanoparticles designed for MPI and other biomedical applications: From synthesis to first *in vivo* studies

Harald Kratz[1]*, Matthias Taupitz[1], Angela Ariza de Schellenberger[1], Olaf Kosch[2], Dietmar Eberbeck[2], Susanne Wagner[1], Lutz Trahms[2], Bernd Hamm[1], Jörg Schnorr[1]

1 Charité –Universitätsmedizin Berlin, Institute of Radiology, Berlin, Germany, **2** Physikalisch-Technische Bundesanstalt, Berlin, Germany

* harald.kratz@charite.de

Citation: Kratz H, Taupitz M, Ariza de Schellenberger A, Kosch O, Eberbeck D, Wagner S, et al. (2018) Novel magnetic multicore nanoparticles designed for MPI and other biomedical applications: From synthesis to first *in vivo* studies. PLoS ONE 13(1): e0190214. https://doi.org/10.1371/journal.pone.0190214

Editor: Raphael Levy, The University of Liverpool, UNITED KINGDOM

Received: June 14, 2017

Accepted: December 11, 2017

Published: January 4, 2018

Data Availability Statement: All relevant data are within the paper and its Supporting Information files.

Funding: The research was supported by the German Ministry for Education and Research (BMBF), Grant No. FKZ 13N11091 and 13N11092, by the German Research Foundation (DFG) research program (quantMPI, grant TR408/9-1 and KFO 213, grant TA 166/7-2) and by grants from the European Fund for Regional Development (EFRE);

Abstract

Synthesis of novel magnetic multicore particles (MCP) in the nano range, involves alkaline precipitation of iron(II) chloride in the presence of atmospheric oxygen. This step yields green rust, which is oxidized to obtain magnetic nanoparticles, which probably consist of a magnetite/maghemite mixed-phase. Final growth and annealing at 90˚C in the presence of a large excess of carboxymethyl dextran gives MCP very promising magnetic properties for magnetic particle imaging (MPI), an emerging medical imaging modality, and magnetic resonance imaging (MRI). The magnetic nanoparticles are biocompatible and thus potential candidates for future biomedical applications such as cardiovascular imaging, sentinel lymph node mapping in cancer patients, and stem cell tracking. The new MCP that we introduce here have three times higher magnetic particle spectroscopy performance at lower and middle harmonics and five times higher MPS signal strength at higher harmonics compared with Resovist®. In addition, the new MCP have also an improved *in vivo* MPI performance compared to Resovist®, and we here report the first *in vivo* MPI investigation of this new generation of magnetic nanoparticles.

Introduction

Having excellent magnetic properties and good biocompatibility, magnetic nanoparticles (MNP) based on magnetite have many technical and biomedical applications [1,2]. Technically, these MNP are used in data storage devices [3], for waste water treatment [4], or as catalysts or supports for catalysts in chemical processes [5,6]. In medical imaging, MNP have been used clinically as both T1 and T2 contrast agents for magnetic resonance imaging (MRI) [7–10]. Other researchers have shown that MNP are also suitable for therapeutic applications including hyperthermia for cancer treatment [11–15] and iron replacement therapy [16]. In regenerative medicine, MNP might be used for stem cell tracking with MRI [17–21]. Most MNP for biomedical applications are coated for colloidal stabilization during or after

and Investitionsbank Berlin (IBB), Grant No. 10146995. The funders had no role in study design, data collection and analysis, decision to publish, or preparation of the manuscript.

Competing interests: The authors have declared that no competing interests exist.

synthesis. Furthermore, MNP coatings can be functionalized with fluorescence dyes, antibodies, or proteins/peptides for bimodal detection of MNP or increased target specificity [22,23]. While MRI is well established, magnetic particle imaging (MPI) is a new emerging imaging modality. This fairly novel biomedical imaging modality is based on the nonlinear magnetization response of MNP to alternating magnetic fields [24] and can directly and specifically display MNP. Compared with MRI, MPI has very high temporal resolution, and a very good signal-to-noise ratio (SNR), allowing quantification of local MNP concentrations [25,26]. MPI can be combined with MRI [27,28] and appears to be particularly well suited for the spatially resolved visualization of rapid dynamic processes in real time such as the beating heart [29–32]. Other applications of MPI may include sentinel lymph node mapping in cancer patients [30,31], passive and active tumor targeting [33], and stem cell tracking [30,34–36]. Resovist® is a liver-specific MRI contrast agent [7,37], that can be used as MPI Tracer and was taken off the market in Europe in 2008. Resovist® has a bimodal magnetic size distribution and only the 30% fraction of larger magnetic cores with an equivalent core size of approx. 22 nm contributes significantly to the MPI signal [38]. Theoretical considerations indicate that single domain MNP with core sizes of about 25–30 nm are best suited for MPI and should be superior to Resovist® [24,39,40]. Therefore, to further exploit the potential of this novel imaging modality, there is a need for improved MPI tracers [33]. The intensity of the MPI signal is dependent on the magnetic moment of the MNP used as tracers [33,38]. In a dispersion of MNP with high magnetic moments, the strong magnetic dipolar interaction between adjacent MNP may decrease colloidal stability. A possible approach to overcome this challenge is to synthesize clusters or so- called magnetic multicore particles (MCP). Because these clusters are composed of individual superparamagnetic cores, they might generate large magnetic moments in a magnetic field if there is sufficient ferromagnetic-like (parallel orientation of individual moments) interaction between single cores/crystals. On the other hand, in zero field the multicore structure might lead to higher colloidal stability in comparison to equivalent singlecore MNP because of the possibility of (partial) flux closure in zero field [38]. In addition, MNP dispersions for biomedical application need to be stable in physiologic media, biocompatible and biodegradable. Especially in vivo biodegradability has not yet been proven for any of the recently developed potential MPI tracers described in the literature [41–44]. Many different methods are available to synthesize iron-oxide-based MNP [1,45], and the most common are coprecipitation and thermal decomposition [1,33]. MNP synthesis using thermal decomposition results in pyrolytic decomposition byproducts of the basic materials due to radical reactions at high temperature(~300˚C) that might hinder possible clinical application because of increased MNP toxicity [46,47]. Here we present a method for simple and reliable synthesis of stable aqueous dispersions of MCP with great potential for MPI, MRI, and other biomedical applications such as drug delivery or hyperthermia treatment.

Results and discussion

Nanoparticle synthesis and characterization

We chose a strongly modified coprecipitation method with relatively mild reaction conditions. Coprecipitation method has proven effective in the development of other iron oxide based drugs and contrast agents [7,20,37,48,49]. However, to obtain monodisperse MNP with high saturation magnetization using this procedure, considerable challenges had to be overcome [50–53]. Especially homogeneous reaction conditions, which are crucial for the formation of monodisperse MNP, are hard to achieve. All ingredients and chemicals that we used had proven biocompatibility and biodegradability and were used in the synthesis of approved medications or contrast agents before [45,54]. Unlike MNP synthesis based on thermal

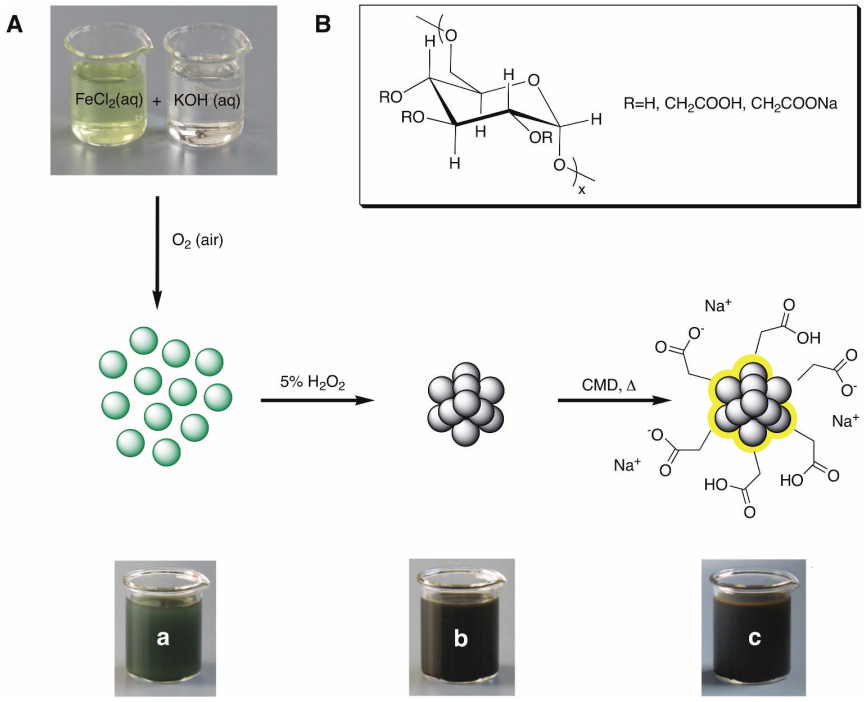

Fig 1. Nanoparticle synthesis. A) Magnetite synthesis with type 1 green rust as intermediate. a) Type 1 green rust—singlecore MNP. b) Fe_3O_4/γ-Fe_2O_3 -MCP. c) CMD-Fe_3O_4/γ-Fe_2O_3 -MCP. B) Carboxymethyl dextran sodium salt (CMD).

https://doi.org/10.1371/journal.pone.0190214.g001

decomposition in organic solvents, the synthesis used here takes place in water and does not require the additional and complex step of phase transfer. The novelty of the developed synthesis presented here is the specific combination of individual steps. The first step of the synthesis method is to coprecipitate iron(II) chloride and KOH in the presence of atmospheric oxygen to obtain type 1 green rust [55–58] (Fig 1), to which hydrogen peroxide is added to yield Fe_3O_4 (magnetite) [59]. Because of the presence of oxygen during synthesis and storage, we assume the particles to consist of Fe_3O_4/γ-Fe_2O_3 (magnetite/maghemite) mixed-phase.

The synthesis parameters were chosen such that the pH of the dispersion following synthesis came close to the point of zero charge (PZC) of magnetite (pH = 6–6.8) [55] and maghemite (pH = 6.6) [60]. The MCP resulting after purification by magnetic separation were supplemented with a large excess of carboxymethyl dextran sodium salt (CMD) and then heated to 90˚C for several hours. Heating, along with the large excess of CMD, aims at ensuring slow, controlled growth by aggregation or oriented attachment [61] of the MCP and partial reduction of γ-Fe_2O_3 to Fe_3O_4. In addition, long heating possibly improves the crystal structure of the MCP through annealing, since the ferrimagnetic properties of magnetite depend on the distribution of Fe^{2+}/Fe^{3+} ions between A-sites and B-sites [62,63]. Another process that might improve the crystal structure is the simultaneous elimination of foreign ionic inclusions or imperfections of the crystal structure resulting from prior oriented attachment [61,64]. CMD coating of our MCP led to electrosteric stabilization, ensuring adequate stability of the MCP in aqueous dispersion at physiologic pH despite MCP large magnetic moments. The functional groups of the CMD coating allow chemical attachment of diverse molecules for further future biomedical applications [23]. The synthesis parameters during the development of MCP were systematically varied to iteratively optimize MCP in terms of signal intensity of the odd-numbered harmonics in magnetic particle spectroscopy (MPS). It turned out that a longer heating

Table 1. Difference between MCP 1 and MCP 2.

MCP	synthesis variant	annealing/ reduction (h)	oxidizing agent 5% H_2O_2 (ml)	magnetic separation
MCP 1	I	7,5	2	dispersion 2
MCP 2-1	II	8	3	dispersion 4
MCP 2-2	II	8	3	dispersion 5

https://doi.org/10.1371/journal.pone.0190214.t001

process after addition of CMD with probable simultaneous annealing and reduction combined with a larger amount of oxidizing agent had a strongly positive impact in the MPS/MPI characteristics. Another important point was the optimization of the magnetic fractionation of the particles under usage of a Base. The main difference between MCP 1 and MCP 2 is the quantity of oxidizing agent used during synthesis (Table 1).

Analysis of the three resulting MCP variants (MCP 1, MCP 2–1 and MCP 2–2) using high-resolution transmission electron microscopy (HRTEM) and the corresponding selected area electron diffraction (SAED) patterns (Fig 2A–2C) showed the MCP presumably to consist of magnetite with a predominantly clustered structure (multicore particles). For evidence of the simultaneous presence of maghemite for example x-ray diffraction (XRD) or Mössbauer investigations would be necessary [65,66].

While HRTEM showed that MCP 1 consisted of two types of MNP, MNP with a clustered structure (multicore particles) and others with an unknown structure (S1 Fig), the other two variants—MCP 2–1 and MCP 2–2 –consisted predominantly of MNP with a clustered structure (S1 Fig). Whereas MCP 1 consists of about 50% clustered particles, MCP 2–2 is composed of about 90% of these. Fig 3 presents the distribution of core sizes determined by TEM, and Table 2 lists the mean core sizes (d and d_V) of the MCP along with other parameters. However, in case of the present MCP the effective domain size, i.e. the size of a domain with the same magnetic moment and the same saturation magnetization, is smaller than the physical size of the MCP. This relationship depends on many parameters like the single core size, its packing fraction, total MCP-size, as well as its inner structure. Another interesting question is, whether it is possible to separate the different kind of particles and do they equally contribute to the MPI signal? Possible methods for the separation are the field-flow fractionation (FFF) [67], or more precise the magnetic field-flow fractionation [68].

To determine the potential of the MCP for MRI applications, we measured their relaxation rates (R1 and R2). The relaxivity coefficient r2, which is a measure of T2-weighted MRI contrast, is experimentally determined by calculating the relaxation rate (R2 = 1/T2) as a function of iron concentration. The spin-spin relaxation rate R2 is roughly proportional to the square of saturation magnetization (M_S) [69,70]. The MCP have r2 values in the range of 300 to 404 l $mmol^{-1}s^{-1}$ (Table 2), which is very high for MCP synthesized from magnetite/maghemite in aqueous dispersion and suggests a high potential for T2- and T2*-weighted MRI applications.

The MCP hydrodynamic sizes were measured by dynamic light scattering (DLS). In DLS measurements no aggregates could be detected (S2 Fig). The long-term stability of the MCP is also very good. In detail the particles dispersions of MCP 1 are stable at least for one year, MCP 2–1 and MCP 2–2 at least for a period of two years. In phosphate-buffered saline (PBS) the colloid is stable for at least 12 hours before aggregation arise. The synthesized MCP have M_S values of 95 to 115 Am^2/kg Fe determined with a superconducting quantum interference device (SQUID) measuring M(H) at 295˚K (Fig 4).

The M(H) curves were analyzed applying a model which describes the magnetization by the superposition of non-interacting MNP with different sizes as described in [38]. Using a lognormal distribution of the MNP diameters, the M(H)-data could not be described successfully. Thus we applied a bimodal lognormal distribution of the magnetic moments as it was

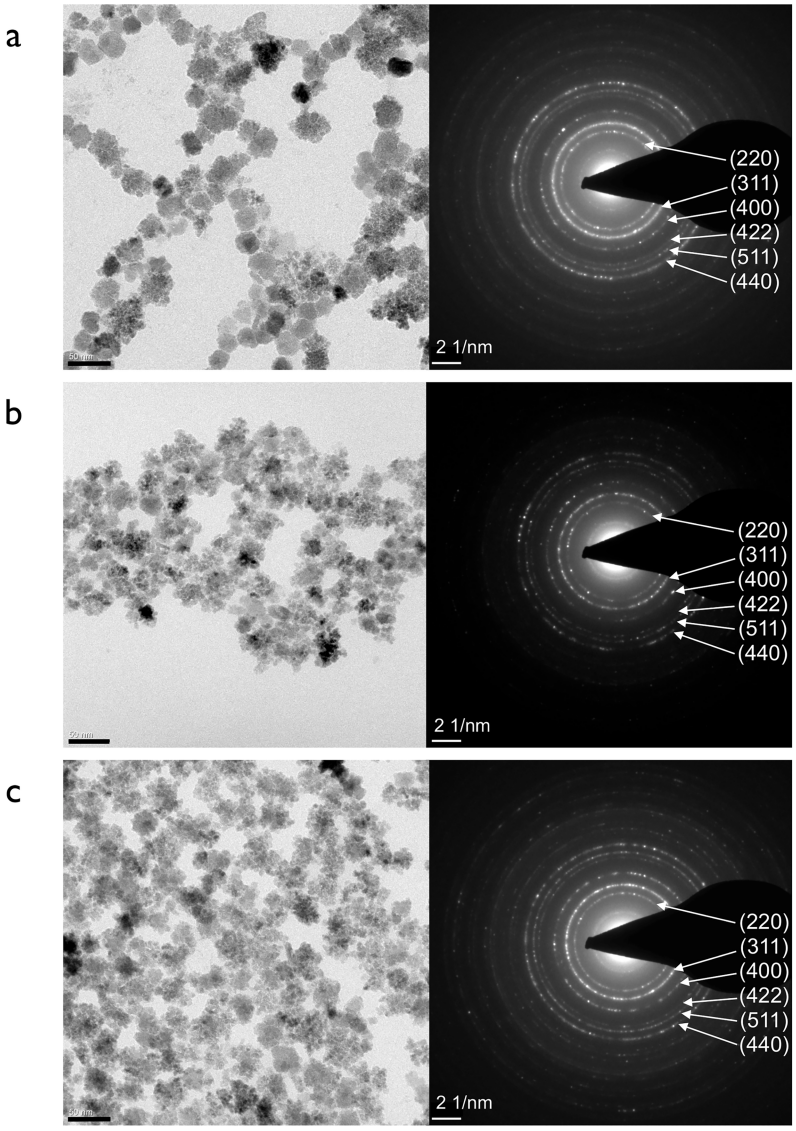

Fig 2. TEM images (scale bar: 50nm) on the left and corresponding SAED patterns (scale bar: 2 nm^{-1}) on the right of (a) MCP 1, (b) MCP 2–1 and (c) MCP 2–2. For magnified TEM images of MCP 1 and MCP 2–2 see supplement.

https://doi.org/10.1371/journal.pone.0190214.g002

found to be necessary also for Resovist [38]. The first mode comprises MNP with diameters smaller about 10 nm, which do not contribute to the MPS or MPI signal significantly [71]. Accordingly, in Table 3 only the parameters of the second, MPS-active mode, are listed.

Assuming a spherical shape of the particles, the distribution of effective magnetic diameters was derived from the magnetic moment distribution in order to get a comparison with diameters of the physical particle (TEM-data). The effective magnetic diameters of the mean magnetic moments or mean magnetic volume of the second mode, d_{v2}, are clearly smaller than the mean physical (TEM-related) diameters. This is obviously attributed to the multicore structure of the MNP leading to a reduced moment in comparison to a singlecore MNP of the same size due to a packing fraction of the magnetic material smaller than one within the multicore MNP. Magnetic interaction among the single magnetic grains obviously creats a large main

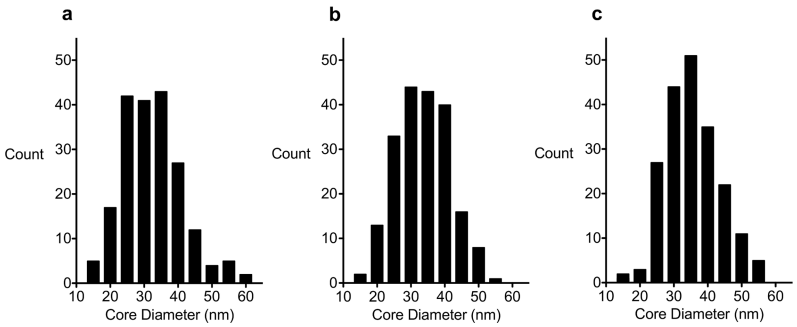

Fig 3. TEM size distributions of (a) MCP 1, (b) MCP 2–1 and (c) MCP 2–2 based on measurement of 200 MCP in each case. The y-axis of the histogram represents the number of particles.

https://doi.org/10.1371/journal.pone.0190214.g003

domain per multicore MNP which contributes to the second mode of the size distribution. This interaction seems to be of exchange nature, because the grains are crystallographically partially grown together (S3 Fig). On the other hand, within the less compact multicore MNP, there also remain smaller magnetic structures i.e. moments of single grains (one domain) or some correlated of them, which do not interact via exchange coupling. These structures seem to be attributed to the first mode of the obtained size distribution, comprising these smaller domains. In HRTEM we could find some indications for that hypothesis (S3 Fig). It seems that there are less dense areas in the multicore particles and sometimes different orientations of the crystal lattice are visible within one particle. Note, that these first hypotheses have to be checked by further investigations harnessing more methods for structure investigation like e.g. small and wide angle X-ray scattering (SAXS, WAXS). The most important parameter, derived from M(H)-data, which determines the MPS performance is the magnetic moment, here the mean of the second mode μ_2. For MCP 2–2, MCP 2–1 and Resovist $\beta\mu_2$ correlates well with the MPS-amplitude at 3rd harmonics M_3 (Table 3). The deviation from this relation for MCP 1 might be attributed mainly to the much larger width of the size distribution σ_2, making a proper comparison difficult because of the nonlinear relationship between moment and MPS signal.

In the literature, M_S bulk values of 111 and 127 Am^2/kg Fe are reported for maghemite and magnetite, respectively [72,73]. Also in literature, aggregates, so-called Nanoflowers are described, which have a similar structure like our MCP in the TEM, but show only a saturation magnetization of about 60 Am^2/kg Fe [74–76]. Actually, the reported saturation magnetization M_S of magnetite/maghemite nanoparticles is generally below pure bulk values [77–81]. This deviation from the bulk values of magnetite/maghemite is attributable to coordination effects of organic ligands [82,83] and/or a crystallographically disordered outer layer of MNP [84], often referred to a magnetic dead layer [85–87]. Hence, the with MCP obtained relatively high

Table 2. Compilation of important properties of the MCP determined by magnetic measurement, TEM and DLS.

Particle	r1 [l mmol^{-1} s^{-1}]	r2 [l mmol^{-1} s^{-1}]	d TEM* [nm]	d_V DLS [nm] by volume	Z-Average [nm]	Pdi
MCP 1	16	300	32.53	24.4-58.8; m	55.0	0.172
MCP 2-1	20	350	33.56	24.4-58.8; m	47.2	0.074
MCP 2-2	17	404	35.31	28.2-68.1; m	52.4	0.083

* 200 MCP counted

https://doi.org/10.1371/journal.pone.0190214.t002

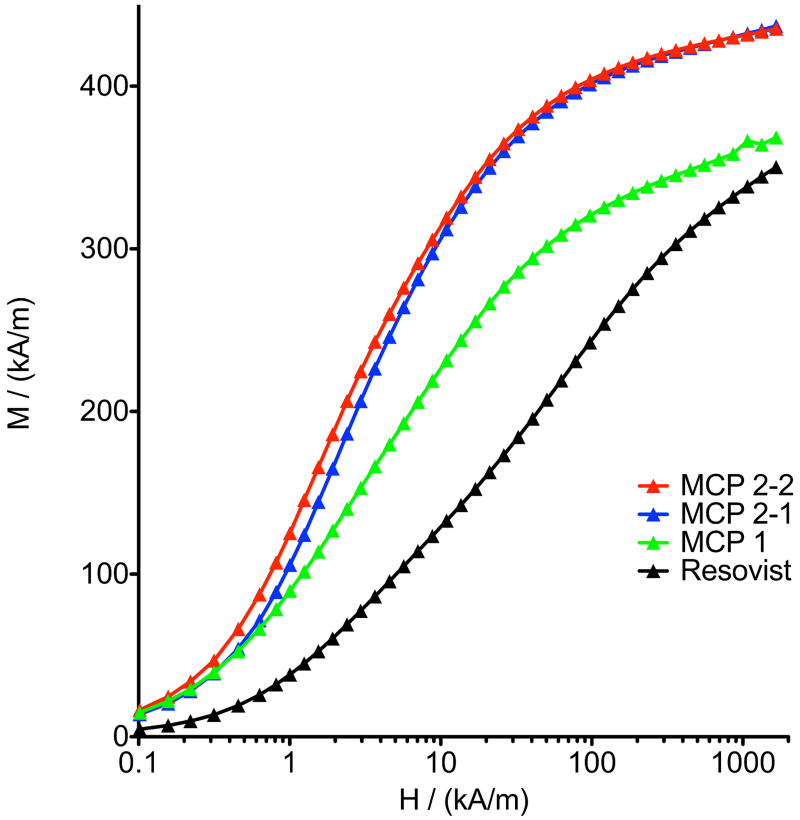

Fig 4. Mass magnetization *M* as a function of applied external field *H* measured for MCP 1, MCP2-1 and MCP2-2 with a SQUID at 295˚C.

https://doi.org/10.1371/journal.pone.0190214.g004

M_s-values in the range of 110 Am^2/kg or above seem to refer to a crystal structure close to that of pure magnetite, i.e. a low amount of crystallographic disorder.

With regard to MPS signal intensity, optimized MCP synthesis also resulted in MCP 2 with higher M_S and a lower polydispersity index (PDI) in comparison with MCP 1. The first step to test whether a new MNP is suitable for MPI is to investigate a specimen by MPS. In MPS, moments of the MNP are driven with a certain frequency in the kilohertz range (25 kHz in our case) when exposed to an alternating magnetic field. As a result of the MNP nonlinear magnetization response, higher harmonics of the basic frequency are generated, which are specific to the MNP and are measured inductively [24]. MPS can be regarded as a zero-dimensional type of MPI scanner without spatial resolution [88]. Resovist® can be considered a gold standard

Table 3. Fit parameters obtained from analysis of the M(H). Here M_s is the saturation magnetization while β, d_{v2}, σ_2, and μ_2 denote the volume fraction, the diameter of mean volume, the dispersion parameter and the mean magnetic moment of the MNP of the second mode of the fitted bimodal lognormal distribution. M_3 is the MPS-amplitude at 3rd harmonics.

Sample	β	d_{v2} [nm]	σ_2	M_s [Am^2/kg Fe]	μ_2 [aAm^2]	$\beta\mu_2$ [aAm^2]	M_3 [Am^2/mol(Fe)]
MCP 1	0.55	15	0.47	95	0.6	0.34	0.30
MCP 2–1	0.70	20	0.26	115	1.9	1.36	0.51
MCP 2–2	0.51	25	0.18	114	3.7	1.88	0.52
Resovist	0.23	24	0.21	98	2.7	0.61	0.20

https://doi.org/10.1371/journal.pone.0190214.t003

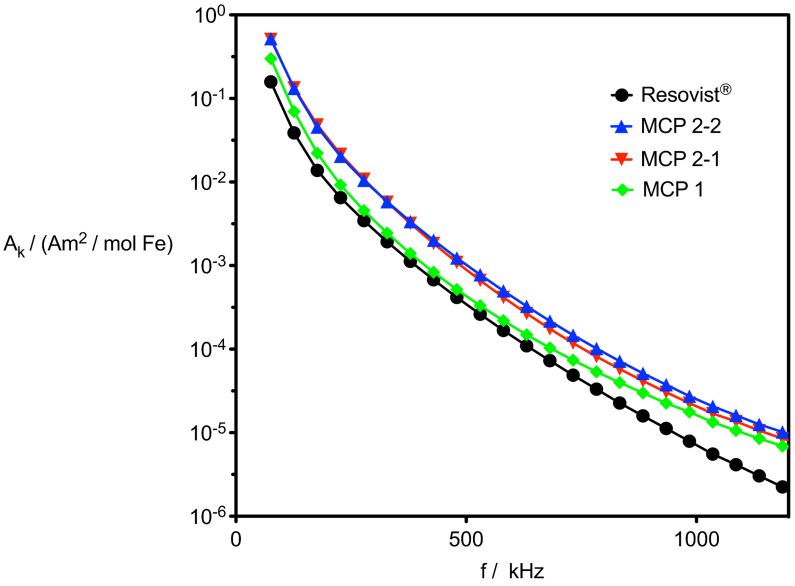

Fig 5. MPS data of MCP 1, MCP 2–1 and MCP 2–2 in comparison with Resovist® (10 mT, 25kHz). Data are plotted as magnetic moment (normalized for iron content) versus frequency. Only odd harmonics are shown, and lines have been added to guide the eye.

https://doi.org/10.1371/journal.pone.0190214.g005

in MPI—it is still the MPI tracer that has been mostly used in vivo [25,89,90] and was commercially available as contrast agent for clinical MRI in the past [91]. The MPS spectra obtained at 25 kHz and 10 mT show that the new MCP are superior to Resovist® in terms of MPS performance (Fig 5). The signal strength of the MCP 1 sample is already superior to Resovist® in the range of lower to middle harmonics of up to approx. 700 kHz, but its relevant superiority is seen at higher harmonics, where the MPS signal intensity of MCP 1 is four times stronger than that of Resovist®. The MPS signal intensities of lower and middle harmonics of MCP 2–1 and MCP 2–2 are three times higher and those at higher harmonics even five-times higher than those achieved by Resovist®.

In vitro investigations

We compared the uptake of MCP 1 and Resovist® by nonphagocytic cells (MSC) and phagocytic macrophages (RAW 264.7) using two protocols, with and without transfection agent (TA). Cationic TAs are commonly used to form positively charged NP complexes to facilitate cell membrane penetration of anionic MNP and increase their uptake by nonphagocytic cells such as MSC [92–95]. However, the use of TA with cells for human cell therapies will require additional FDA evaluation of the MNP-TA complex [96]. Therefore, alternative methods that avoid the use of TA are relevant for medical translation [21]. For this reason, we compared MCP 1 uptake with and without TA and in MSC. Although, phagocytic cells do not require protamine sulfate for MNP uptake, equal protocols were tested with RAW 264.7 macrophages for consistent comparison. Furthermore, the methodology used to achieve MNP-intracellular uptake was improved by removal of extracellular MNP. The quantification of the average intracellular MNP uptake was done by iron quantification and visualization by iron stain as previously published in our group [21]. In vitro biocompatibility of MCP 1 was tested after MNP uptake by mesenchymal stem cells (MSC) and macrophages (RAW 264.7) (S4 Fig and S5 Fig) for their effect on cell proliferation in comparison with unlabeled cells and cells labeled with Resovist®.

Mesenchymal stem cells. Overall, MSC were more efficiently labeled with MCP 1 than with Resovist® with protamine sulfate as cationic transfection agent (TA) (0.2 mM: TA and 1 mM: TA) and without TA (0.2 mM). The use of TA increased the average intracellular uptake of MCP 1 (8- to 13-fold), resulting in average uptake of 10 pg Fe/cell (at 0.2 mM: TA; MNP loading concentration) and 15 pg Fe/cell (at 1 mM: TA; MNP loading concentration. Although the increase in MNP uptake with TA is higher for Resovist® (16- to 26-fold with TA) than for MCP 1 (8- to 13-fold). The highest MSC uptake was achieved with MNP loading concentration of 1 mM: TA) with average MCP 1 uptake of 13 pg Fe/cell and average Resovist® uptake of 9 pg Fe/cell (S4 Fig).

Macrophages (RAW 264.7). Overall, this phagocytic cell line showed higher uptake of MCP than Resovist® as confirmed by iron quantification after removal of extracellular iron (S5 Fig). Slight higher uptake of MCP 1 was observed with 0.2 mM MNP loading concentration without TA (~12 pg Fe/cell) than with TA (~8 pg Fe/cell). However, a higher MNP loading concentration (1mM) with TA significantly increased intracellular average MNP uptake by macrophages for both MCP 1 (up to 265 pg Fe/cell)) and Resovist® (65 pg Fe/cell) (S5 Fig), As expected, overall uptake of MCP 1 and Resovist® was higher in the phagocytic macrophage cell line (RAW 264.7) than in MSC. The uptake of MCP 1 was higher than that of Resovist® independent of cell type and use of cationic TA. The negative charge of CMD coating of MCP 1 is stronger than that of carboxydextran coating of Resovist®. This might explain the higher affinity of MCP 1 to cationic TA and the higher cellular uptake of MCP 1 in comparison to Resovist® as later discussed. In addition, MNP uptake increased with increasing MNP loading concentration with TA (S6 Fig, S7 Fig and S8 Fig).

We observed that larger complexes are formed by incubation of MCP 1 with TA than with Resovist® in cell culture conditions (S6 Fig and S7 Fig). Larger MCP 1-TA complexes might be one reason for increased uptake for MCP 1-TA in comparison with the uptake for Resovist®-TA. Although, MCP 1 and Resovist® are both sterically stabilized. Resovist® is coated with carboxydextran and MCP 1 with carboxymethyl dextran (CMD). The additional CMD groups in MCP 1 accounts for their larger zeta potential (-32.8 mV) in comparison with Resovist® (-25.1 mV). A larger surface charge of MCP 1 can increase the interaction with positive charged proteins such as fetal bovine serum (FBS) but also cell membrane components. These can cause that MCP 1-protein corona is formed, which can influence NP uptake. The addition of TA had a larger effect on uptake of MCP 1 for macrophages than for MSC (S4 Fig and S5 Fig) (FACTORS correspondently). Suggesting two different mechanisms for MCP 1-TA uptake in MSC and macrophages. Considering that the formation of a MNP protein corona not only influences uptake by cells but MNP stability [97]. We observed that the well plates where cells were incubated without TA, remained free of MNP-TA aggregates (S6 Fig: e—h for MSC and S7 Fig: e—h for macrophages), suggesting better MCP 1 stability when TA was avoid. In addition, MCP 1 uptake was increased in both cells by increasing MNP loading concentration to 1mM. Although the cellular mechanisms for MCP 1 uptake are beyond the scope of this manuscript. We speculate an endocytosis-independent pathway by diffusion for the internalization of MCP 1-TA (S6 Fig and S7 Fig). Future investigations will be required to prove this theory by comparing MCP 1-TA uptake in presence of inhibitors for the endocytic pathways [98]. Overall, the protocol for cellular uptake of MCP 1, is improved by increasing MCP 1 loading concentration to 1 mM, elimination of the use of TA, and inclusion of ECM digestion to remove extracellular MCP 1. This methodology provides an improved protocol for intracellular labeling of MSC with MCP 1 and Resovist [21] and macrophages with MCP 1 as shown in this manuscript. The reduction of extracellular MCP 1 by ECM digestion and cell passage is exemplarily shown for MCP 1 at 0.2 mM and 1mM loading concentrations in supplementary S8 Fig (S8 Fig).

Effect of MCP on the proliferation of MSC and macrophages. The effect of MCP 1 on MSC proliferation was tested over 12 days by measurement of population doubling time (PDT) of MCP 1-labeled cells and compared with the PDT of Resovist®-labeled and unlabeled cells. Despite the higher uptake of MCP 1 in comparison with Resovist®, the PDT of both MSC and macrophages was similar for cells labeled with MCP 1 and Resovist® in comparison with unlabeled cells (S9 Fig). Additional studies published by our group confirm that MCP efficiently label MSC, enabling MRI with single cell sensitivity. Furthermore, MCP -labeled MSC maintained their in vitro stem-cell-like character, and features such as colony-forming unit capacity, in vitro multilineage differentiation capacity (adipogenesis, chondrogenesis and osteogenesis), and expression of MSC surface markers (CD90, CD44, CD73 and CD133) remained unmodified [21]. These findings further support the in vitro biocompatibility of MCP with MSC. Further experiments such as migration assays for MSC and investigations to test the immune responsiveness of macrophages should be performed with a view to specific biomedical applications of MCP 1-labeled cells. In addition, longitudinal measurements of MRI but also MPS and MPI signal will be required to confirm in vivo the stability of MNP in intracellular compartments. Two possible applications of MCP deserve special mention. First the uptake of MCP 1 by MSC is increased in comparison with Resovist® and their detectability by MPI should be further explored. Second, higher uptake of MCP 1 than Resovist® by macrophages should be carefully evaluated for applications that include intravenous systemic application. However, good uptake of MCP 1 by macrophages could in the future be exploited for specific imaging and theranostic targeting of macrophage-associated diseases [99], and these applications should also be explored for new generation MPI-MNP such as MCP 1.

First *in vivo* studies and MRI experiments

MRI was used to determine the blood half-life of MCP 1 in rats. A total of 6 Sprague Dawley® rats (SD rats, Charles River, Sulzfeld, Germany) were examined by T1-weighted and T2*-weighted MRI. The effect of MCP 1 was a transient signal enhancement within the vasculature in T1 weighted MRI and a signal decrease of the liver parenchyma in T1 and T2 weighted MRI, due to the well-known uptake of nanoparticles by phagocytic cells in the liver. The T1 weighted MRI blood half-life of MCP 1 was 8.8 and 17.4 min at 50 and 100 μmol Fe/kg, respectively, as measured using serial T1 weighted MRI (Figs 6 and 7).

Duration of degradation of MCP 1 in the liver, as measured using T2*-weighted MRI, was 5 weeks with a half-life of 7 days. Please note that MRI is not quantitative. A total of 4 Spraque Dawley (SD) rats (Charles River, Sulzfeld, Germany) were examined for *in vivo* compatibility. MCP 1 *in vivo* compatibility was studied using doses of up to 3 mmol Fe/kg of body weight, and overall no adverse effects such as reduced motility or piloerection were observed.

Initial *in vivo* MPI experiments. To study the MPI behavior of MCP 2–2 in a preclinical MPI scanner (Bruker Biospin GmbH, Ettlingen, Germany) [28], a total of 2 SD rats (Charles River, Sulzfeld, Germany) were examined using Resovist® and MCP 2–2 with doses of 0.1 mmol Fe/kg and 0.05 mmol Fe/kg, respectively. These in vivo experiments showed high intravascular MPI signal intensities, allowing adequate evaluation of the images. These initial experiments also showed MCP 2–2 to have good imaging properties. A direct comparison of *in vivo* MPI data of MCP 2–2 and Resovist® using the same reconstruction parameters revealed the superiority of our newly developed MPI-Tracer (MCP 2–2) over Resovist® in terms of higher S/N and better anatomical delineation of the blood vessel (Figs 8 and 9). A method for accurate co-registration of MPI and MRI data is currently being developed. Another interesting aspect would be the comparison with LS-008 tracer (LodeSpin, Seattle, USA). These Particles showed a mean amplification of amplitudes of 3.4 compared to Resovist in MPS at 14 mT and 25 kHz

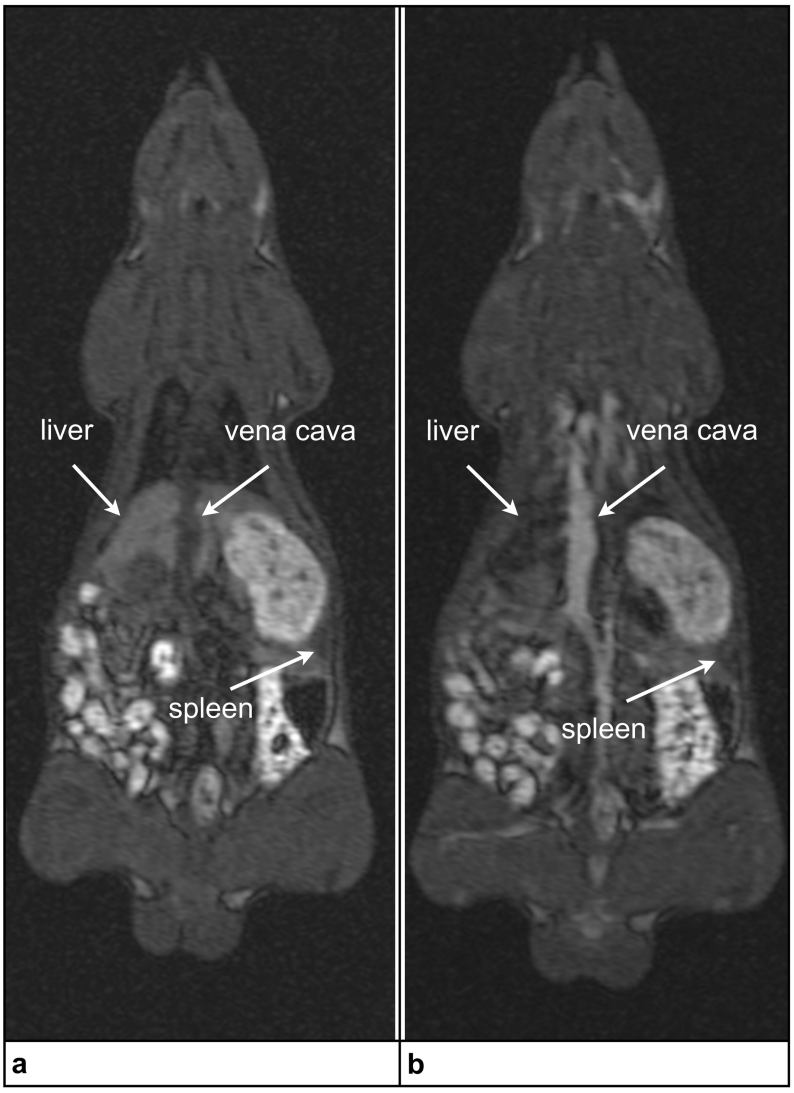

Fig 6. *In vivo* MRI at 1.5 Tesla: T1-weighted 3D gradient-echo (GRE) fast low angle shot sequence. a–Image without administration of MCP 1; b–Image obtained 2 minutes after administration of 0.1 mmol Fe/kg of MCP 1.

https://doi.org/10.1371/journal.pone.0190214.g006

and a better spatial MPI resolution [100]. Because of its polyethylene glycol (PEG) coating LS-008 shows a long circulation time and is used as a blood pool tracer [44,100].

Conclusions and outlook

In summary, we present a novel aqueous synthesis for generating MCP with excellent magnetic characteristics, and therefore highly suited for both MRI and MPI, and could allow the combination of these two techniques for bimodal imaging. The innovation of the new synthesis lies in the oxidation of green rust to a probably magnetite/maghemite mixed-phase in conjunction with subsequent annealing and parallel partly reduction at 90˚C for several hours. Our results indicate, that MCP containing aggregates composed of uniform small single crystals lead to improved MPI performance. Experimental MPS and *in vivo* MPI data demonstrate the superior performance of MCP in comparison with Resovist®. In addition we show that

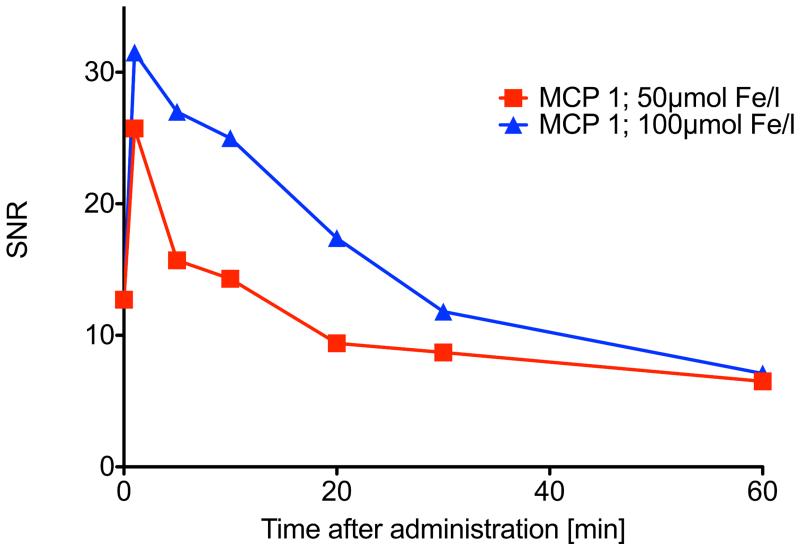

Fig 7. T1 weighted MRI blood half-life measurement of MCP 1 (50 and 100µmol Fe/kg) at 1.5 Tesla: T1-weighted 3D gradient-echo (GRE) fast low angle shot sequence.

https://doi.org/10.1371/journal.pone.0190214.g007

MCP 1 is in vitro biocompatible after intracellular uptake and can be used to efficiently label cells to further study their potential for in vivo cell tracking by MRI and MPI in regenerative medicine and stem cell therapies. Furthermore, MCP 1 did not have in vivo adverse effects at doses of up to 3 mmol Fe/kg body weight, and showed a liver half-life of about 7 days. Because MCP 1 and MCP 2 have the same CMD coating and the same basic core structure, we assume that these MNP also have similar in vitro and in vivo characteristics. Nevertheless, further

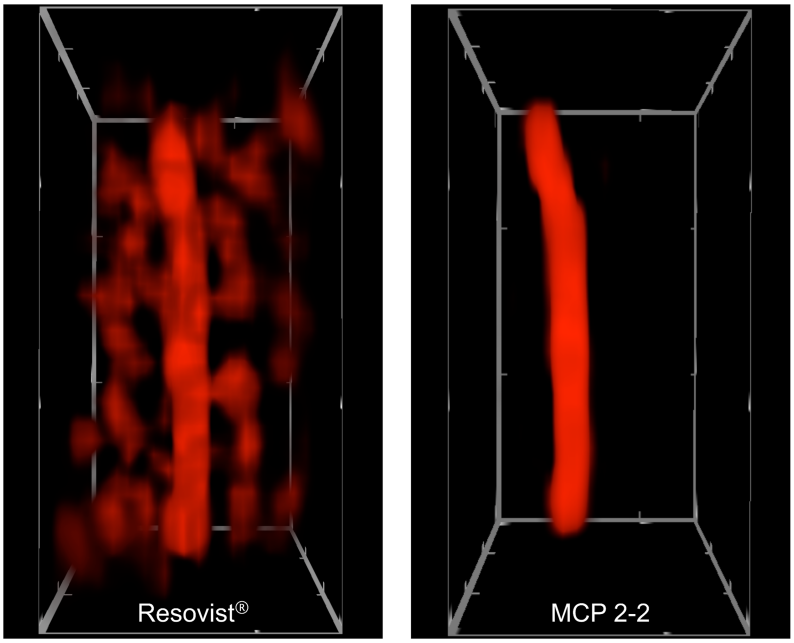

Fig 8. *In vivo* MPI image of vena cava of a rat after i.v. bolus administration of 0.05 mmol Fe/kg (0.1 ml) Resovist (left) and MCP 2–2 (right) respectively. For both image reconstructions the same parameters were used. 3D volume of field of view (FOV) with a size of 28 x 28 x 14 mm^3 is shown.

https://doi.org/10.1371/journal.pone.0190214.g008

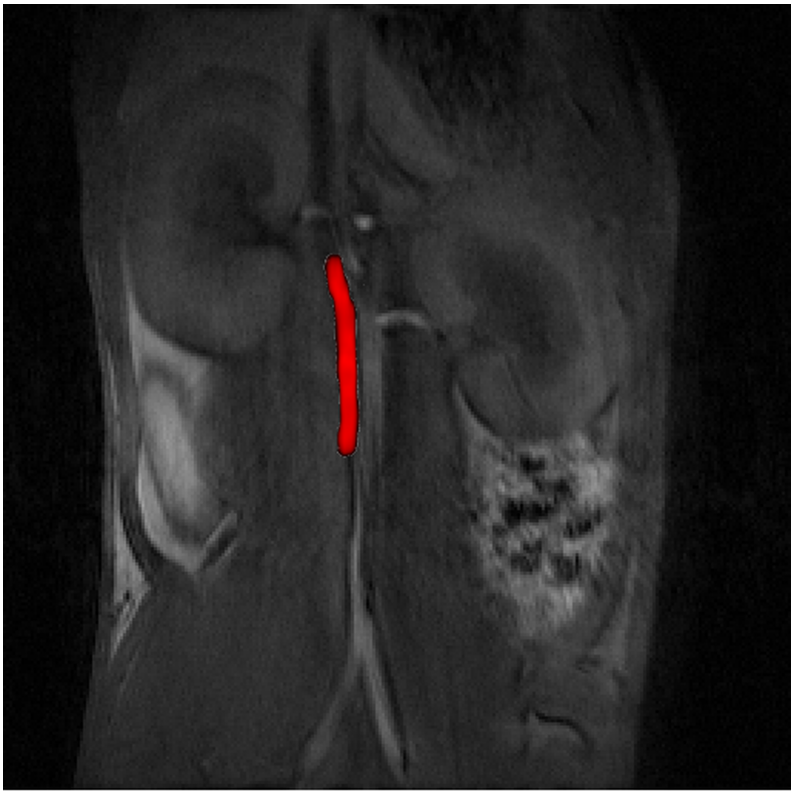

Fig 9. *In vivo* MRI image at 1.0 Tesla (ICON MRI, Bruker): T1-weighted 2D gradient-echo (GRE) fast low angle shot sequence overlaid with 3D volume *in vivo* MPI image of Fig 8 of the same rat.

https://doi.org/10.1371/journal.pone.0190214.g009

investigations are required to test the in vitro and in vivo properties of MCP 2 in more detail. The presented initial MPI experiments for imaging the vena cava of rats are the first in vivo MPI studies using MCP 2–2 as improved MPI tracers of a new generation synthesized by coprecipitation. The next challenge is to show that the new MPI tracers are suitable for cardiovascular imaging and further biomedical applications such as sentinel lymph node mapping in animal models of cancer or stem cell tracking. Further efforts will aim at optimizing the pharmaceutical formulation of MCP and increase specificity by functionalization of the MCP coating, e.g., with antibodies for targeted imaging or with drugs for specific uses as theranostics.

Experimental section

Materials and instruments

All chemicals were purchased from Sigma-Aldrich (Steinheim, Germany). Iron(II) chloride tetrahydrate, carboxymethyl dextran sodium salt and potassium hydroxide were used as received. To prepare 5% hydrogen peroxide solution (5 wt % in H_2O), hydrogen peroxide solution (30 wt % in H_2O) was diluted with five (5) parts of deionized water. Deionized water was produced using a Mill-Q A10 system (Millipore, Billerica, MA, USA). The ferric and ferrous iron content of the particle dispersions was colorimetrically determined using the phenanthroline method [101].

Preparation of multicore particles

For synthesis of MCP (MCP 1 and MCP 2), Fe(II)chloride tetrahydrate was dissolved in deionized water under an air atmosphere, and potassium hydroxide and hydrogen peroxide were

successively added under stirring. The resulting MCP were washed with water by magnetic separation, and carboxymethyl dextran sodium salt (CMD-Na) was added and solved under stirring. The mixture was diluted with water and heated at 90˚C for 7.5–8 h. Thereafter, several magnetic separation steps were performed to remove the sediment, and the supernatants were combined and washed with water via ultrafiltration and concentrated. The resulting aqueous dispersions were divided into fractions by magnetic separation using water and occasionally KOH solution to obtain the final MCP. For in vivo use, the MCP were concentrated by centrifugation with centrifugal filter units. To the resulting dispersion, D-mannitol and optionally aqueous sodium lactate were added to adjust the pH of the dispersion to a range of 6.5 to 7.5, followed by sterile filtration (syringe filter) and autoclaving. (For details of the reaction, see S1 Protocol).

Nanoparticle characterization

Nanoparticle size and morphology were analyzed by high-resolution transmission electron microscopy (HRTEM) using a TECNAI G2 20 S-Twin (FEI-Company, Hillsboro OR, USA).

Average core/multicore diameters (d_v) and size distributions were calculated for each nanoparticle sample by averaging 200 particles from the TEM images using ImageJ software (developed by the National Institutes of Health, Bethesda, Maryland, USA). The hydrodynamic diameters of the MNP were determined by dynamic light scattering (DLS, also referred to as photoelectron correlation spectroscopy, PCS) on a Zetasizer Nano ZS particle analyzer (Malvern Instruments, Worcestershire, UK). For Zetasizer measurement, MNP dispersions were diluted with water to a final concentration of 1 mmol Fe/l. T_1- and T_2-relaxivities were measured with a Minispec MQ 40 Time-Domain Nuclear magnetic resonance (TD-NMR) spectrometer at 40˚C, 40 MHz and 0.94 T (Bruker, Karlsruhe, Germany). Relaxation coefficients r2 were determined by linear fitting of R2-relaxation rates in relation to iron concentrations.

Ultrafiltration of nanoparticles

Ultrafiltration was performed using Vivaflow 200 filters with a 100 kDa regenerated cellulose (RC) membrane (Sartorius AG, Göttingen, Germany).

MPS and M(H) characterization of nanoparticles

MPS characterization of MCP was performed with undiluted samples in a magnetic particle spectrometer (MPS) (Bruker Biospin, Germany) at 10 mT, 25.2525 kHz and 37˚C for 10 s. For comparison, Resovist® was diluted with water to give 100 mmol Fe/l and measured under the same conditions. For measurement the samples were filled in Life Technologies polymerase chain reaction (PCR) tubes with sample volumes of 30 **μ**l. The amplitude of the magnetic moment, A_k, was normalized to the iron content of each sample and is given in Am^2/mol Fe. M(H) measurements were performed in a 75 **μ**l sample filled in a polycarbonate capsule. The magnetic moment of each sample was measured while increasing the applied magnetic field from 0 to 5 T using an MPMS (Magnetic Property Measurement System, Quantum Design, USA). The background signal caused by empty capsules, diamagnetic susceptibility of the dispersion medium, and demineralized water, was subtracted from the signal obtained for the samples. The magnetization curve was obtained by normalizing the magnetic moment of the sample to its iron content.

In vitro experiments

Cellular uptake of MNP. *In vitro* cellular uptake of MCP 1 was tested with nonphagocytic primary mesenchymal stem cells (MSC) from murine (C57BL/6) BM (Thermo Fisher Scientific, Waltham, MA, USA) and a phagocytic murine leukemic macrophage cell line (RAW

264.7) (ATCC Cell Biology Collection, Manassas, Virginia USA). Cells were maintained for up to ten passages as suggested by providers. All in vitro experiments compared cells labeled with MCP 1 or Resovist® vs unlabeled cells. The protocols used to obtained intracellular labeled MSC were previously published by our group [21], and similar protocols were used for RAW 264.7 macrophages for comparison. In short, cells were transferred into 6-well plates (4,000 cells/cm^2), followed by overnight cell synchronization in growth medium. Cells were labeled with MCP 1 or Resovist® using MNP loading concentrations of 0.2 mM or 1 mM with (MCP 1:TA or Resovist®:TA) or without protamine sulfate as cationic transfection agent (TA). Cells were incubated with MNP for 24h in corresponding cell culture medium with 1% FBS for culture synchronization [102]. MNP incubation with cells was followed by three washing steps using phosphate-buffered saline (PBS) and collected for iron stain (S6 Fig and S7 Fig) or cell passage into a new 6-well plate (4000 cells/cm^2). This last step was included to completely remove extracellular MNP and MNP adherent to cell culture plastic material [21]. Cell pellets were collected after removal of extracellular MNP and MNP-intracellular uptake was confirmed by iron staining using a Prussian blue protocol (S8 Fig). Replicates (n = 3) from cell pellets equally treated were used for Fe quantification of intracellular MNP by the colorimetric phenanthroline method described somewhere else [103,104] with some modifications for cell pellets and read at 510 nm. Detailed protocol for cell pellets haven been previously described in our group [21]. The mean MNP uptake was calculated from different experiments (n = 3). Fe concentration was calculated using a standard curve from iron standards with 0, 1, 2, 4, 6, 8, 10, 14 and 18 mg Fe /mL. The mean MNP uptake was normalized to cell number and is reported for MSC (S4 Fig) and for macrophages (S5 Fig).

Effect of MCP 1 uptake on cell proliferation. Population doubling time (PDT) was assessed as described elsewhere [21,105]. In short, labeled and unlabeled MSC and RAW 264.7 (S9 Fig) were plated into six-well plates at 2,000 cells per well with complete growth medium and the medium was exchanged every 2 days. The cell population was quantified every 2 days for up to 12 days by automatic cell counting with the CASY Model TT. The following formula was used to calculate the PDT: PDT = T x ln2/ln(N_t/N_0), where N_0 = initial cell number, N_t = final cell number, and T = time interval.

In vivo MRI and MPI experiments

Rats were maintained in Type IV Macrolon® cages (Zoonlab, Castrop-Brauxel, Germany) on softwood granulate (Lignocel, J. Rettenmaier, Rosenberg, Germany) under a constant 12-h day/night cycle, a temperature of 21 ± 1˚C, and 50 ± 5% relative humidity according to the recommendation *2007/526/EC* of the European Commission. Animals received commercial standard pellet feed (ssniff, R-M-H, Soest, Germany) and tap water ad libitum. In vivo experiments in rats were conducted in accordance with the requirements and guidelines of EU directive 2010/63/EU and the German Animal Protection Act. The experiments were approved by the local animal protection committee of the LAGeSo Berlin, Germany. Male rats of the Sprague Dawley® Rat strain (Charles River Laboratories, Sulzfeld, Germany) with a body weight of 300±25 g were examined. Rats were anesthetized prior to and during the imaging procedure using 1.0%–2.5% isoflurane. First MRI examinations were performed on a 1.5 Tesla whole body MRI scanner (Magnetom Sonata; Siemens, Erlangen, Germany) using a commercially available extremity coil. The rats were placed supine on a Styrofoam support and positioned in the center of the coil. Dynamic imaging was performed using a T1-weighted 3D gradient-echo (GRE) fast low-angle shot sequence 2 min after administration. The MNP dispersion was injected into a lateral tail vein as a bolus over 2 seconds. In vivo MPI experiments were performed on a preclinical MPI scanner Bruker 25/20 (Bruker Biospin GmbH, Ettlingen, Germany) at Charité. The

standard MPI system 25/20 implements dual-purpose coils to generate the drive-field (DF) for excitation of the nanoparticle dispersion and to receive the induced voltage signals from the magnetization of these MNP simultaneously. In addition a prototype of a separate coil to receive only was manufactured and installed by Bruker in the MPI system at Charité in the x-axis channel to gain up the signal-to-noise-ratio (SNR) [106]. In the MPI measurement, we applied a DF amplitude of 12 mT in all three directions and a selection field gradient of (Gx/Gy/Gz) = (1.25/1.25/2.5) T/m. Following acquisition, images were reconstructed with a matrix of 32x32x16 and a field of view (FOV) of 28x28x14 mm^3. We have applied a moving average of 5 to the measurement data. The reconstruction is made with the same number of frequency components. Overall 1696 frequency components/equations were selected for both particle systems by choosing the SNR-threshold to 20.77 for MCP 2–2 and 8 for Resovist®. In the reconstruction, we have used the Kaczmarz's algorithm [107] with 5 iterations and a regularization factor of 10^{-5}. The nanoparticle dispersion was injected as a bolus into a tail vein, and MPI acquisition started approx. 1 min before injection. MRI examinations for overlaying MPI and MRI images were performed after corresponding MPI experiments on a 1 Tesla ICON small animal MRI scanner (Bruker Biospin GmbH, Ettlingen, Germany) and a T1-weighted 2D gradient-echo (GRE) fast low angle shot sequence in coronary direction was used. For both, the MPI and MRI examinations a compatible small animal carrier (Bruker Biospin GmbH, Ettlingen, Germany) was used.

Supporting information

S1 Fig. TEM images of MCP 1 and MCP 2–2.
(PDF)

S2 Fig. DLS size distributions (intensity) of MCP.
(PDF)

S3 Fig. HRTEM images for structural considerations.
(PDF)

S4 Fig. MCP 1 uptake by MSC.
(PDF)

S5 Fig. MCP 1 uptake by macrophages.
(PDF)

S6 Fig. Prussian blue stain for mesenchymal stromal cells (MSC) labeled with multicore particles (MCP 1) and Resovist.
(PDF)

S7 Fig. Prussian blue stain for macrophages cell line (RAW 264.7) labeled with multicore particles (MCP 1) and Resovist.
(PDF)

S8 Fig. Prussian blue stain for mesenchymal stromal cells labeled with multicore particles (MCP 1).
(PDF)

S9 Fig. Population doubling time (PDT).
(PDF)

S1 Protocol. Nanoparticle synthesis and formulation procedure of MCP 1 and MCP 2.
(PDF)

Acknowledgments

We thank Bettina Herwig for language editing, Norbert Löwa from the PTB for the fruitful discussion, Monika Ebert for her great support and Sören Selve for TEM investigations at ZELMI (TU Berlin).

Author Contributions

Conceptualization: Harald Kratz.

Funding acquisition: Matthias Taupitz, Lutz Trahms, Bernd Hamm, Jörg Schnorr.

Investigation: Harald Kratz, Angela Ariza de Schellenberger, Olaf Kosch, Dietmar Eberbeck, Jörg Schnorr.

Methodology: Harald Kratz, Angela Ariza de Schellenberger, Olaf Kosch, Dietmar Eberbeck, Susanne Wagner, Jörg Schnorr.

Project administration: Jörg Schnorr.

Validation: Harald Kratz, Angela Ariza de Schellenberger, Olaf Kosch, Dietmar Eberbeck.

Writing – original draft: Harald Kratz, Angela Ariza de Schellenberger, Dietmar Eberbeck.

Writing – review & editing: Matthias Taupitz, Olaf Kosch, Jörg Schnorr.

References

1. Lu AH, Salabas EL, Schüth F. Magnetic nanoparticles: Synthesis, protection, functionalization, and application. Angew Chem Int Ed Engl 2007; 46(8):1222–44. https://doi.org/10.1002/anie.200602866 PMID: 17278160
2. Jun YW, Seo JW, Cheon J. Nanoscaling laws of magnetic nanoparticles and their applicabilities in biomedical sciences. Acc Chem Res 2008, Feb; 41(2):179–89. https://doi.org/10.1021/ar700121f PMID: 18281944
3. Hyeon T. Chemical synthesis of magnetic nanoparticles. Chemical Communications 2003, Apr 3 (8):927–34.
4. Xu P, Zeng GM, Huang DL, Feng CL, Hu S, Zhao MH, et al. Use of iron oxide nanomaterials in wastewater treatment: A review. Sci Total Environ 2012, May 1; 424:1–10. https://doi.org/10.1016/j.scitotenv.2012.02.023 PMID: 22391097
5. Munoz M, de Pedro ZM, Casas JA, Rodriguez JJ. Preparation of magnetite-based catalysts and their application in heterogeneous fenton oxidation–A review. Applied Catalysis B: Environmental 2015, Oct; 176–177:249–65.
6. Gawande MB, Branco PS, Varma RS. Nano-magnetite (fe3o4) as a support for recyclable catalysts in the development of sustainable methodologies. Chem Soc Rev 2013, Apr 21; 42(8):3371–93. https://doi.org/10.1039/c3cs35480f PMID: 23420127
7. Reimer P, Balzer T. Ferucarbotran (resovist): A new clinically approved res-specific contrast agent for contrast-enhanced MRI of the liver: Properties, clinical development, and applications. Eur Radiol 2003, Jun; 13(6):1266–76. https://doi.org/10.1007/s00330-002-1721-7 PMID: 12764641
8. Schnorr JR, Wagner S, Abramjuk C, Drees R, Schink T, Schellenberger EA, et al. Focal liver lesions: SPIO-, gadolinium-, and ferucarbotran-enhanced dynamic t1-weighted and delayed t2-weighted MR imaging in rabbits 1. Radiology 2006; 240(1):90–100. https://doi.org/10.1148/radiol.2393040884 PMID: 16684917
9. Wagner M, Wagner S, Schnorr J, Schellenberger E, Kivelitz D, Krug L, et al. Coronary MR angiography using citrate-coated very small superparamagnetic iron oxide particles as blood-pool contrast agent: Initial experience in humans. J Magn Reson Imaging 2011, Oct; 34(4):816–23. https://doi.org/10.1002/jmri.22683 PMID: 21769977
10. Wang YX. Superparamagnetic iron oxide based MRI contrast agents: Current status of clinical application. Quant Imaging Med Surg 2011, Dec; 1(1):35–40. https://doi.org/10.3978/j.issn.2223-4292.2011.08.03 PMID: 23256052

11. Jordan A, Scholz R, Maier-Hauff K, Johannsen M, Wust P, Nadobny J, et al. Presentation of a new magnetic field therapy system for the treatment of human solid tumors with magnetic fluid hyperthermia. J Magn Magn Mater 2001; 225(1):118–26.
12. Kobayashi T. Cancer hyperthermia using magnetic nanoparticles. Biotechnology Journal 2011; 6 (11):1342–7. https://doi.org/10.1002/biot.201100045 PMID: 22069094
13. Laurent S, Dutz S, Häfeli UO, Mahmoudi M. Magnetic fluid hyperthermia: Focus on superparamagnetic iron oxide nanoparticles. Adv Colloid Interface Sci 2011, Aug 10; 166(1–2):8–23. https://doi.org/10.1016/j.cis.2011.04.003 PMID: 21601820
14. Hergt R, Dutz S, Müller R, Zeisberger M. Magnetic particle hyperthermia: Nanoparticle magnetism and materials development for cancer therapy. Journal of Physics: Condensed Matter 2006, Sep 27; 18(38):S2919–34.
15. Thiesen B, Jordan A. Clinical applications of magnetic nanoparticles for hyperthermia. Int J Hyperthermia 2008, Sep; 24(6):467–74. https://doi.org/10.1080/02656730802104757 PMID: 18608593
16. Kowalczyk M, Banach M, Rysz J. Ferumoxytol: A new era of iron deficiency anemia treatment for patients with chronic kidney disease. J Nephrol 2011; 24(6):717–22. https://doi.org/10.5301/jn.5000025 PMID: 21956770
17. Andreas K, Georgieva R, Ladwig M, Mueller S, Notter M, Sittinger M, Ringe J. Highly efficient magnetic stem cell labeling with citrate-coated superparamagnetic iron oxide nanoparticles for MRI tracking. Biomaterials 2012, Jun; 33(18):4515–25. https://doi.org/10.1016/j.biomaterials.2012.02.064 PMID: 22445482
18. Cromer Berman SM, Walczak P, Bulte JW. Tracking stem cells using magnetic nanoparticles. Wiley Interdiscip Rev Nanomed Nanobiotechnol 2011; 3(4):343–55. https://doi.org/10.1002/wnan.140 PMID: 21472999
19. Edmundson M, Thanh NT, Song B. Nanoparticles based stem cell tracking in regenerative medicine. Theranostics 2013; 3(8):573–82. https://doi.org/10.7150/thno.5477 PMID: 23946823
20. Li L, Jiang W, Luo K, Song H, Lan F, Wu Y, Gu Z. Superparamagnetic iron oxide nanoparticles as MRI contrast agents for non-invasive stem cell labeling and tracking. Theranostics 2013; 3(8):595–615. https://doi.org/10.7150/thno.5366 PMID: 23946825
21. Ariza de Schellenberger A, Kratz H, Farr T, Loewa N, Hauptmann R, Wagner S, et al. Labeling of mesenchymal stem cells for MRI with single-cell sensitivity. Int J Nanomedicine 2016, Apr:1517. https://doi.org/10.2147/IJN.S101141 PMID: 27110112
22. Sapsford KE, Algar WR, Berti L, Gemmill KB, Casey BJ, Oh E, et al. Functionalizing nanoparticles with biological molecules: Developing chemistries that facilitate nanotechnology. Chemical Reviews 2013; 113(3):1904–2074. https://doi.org/10.1021/cr300143v PMID: 23432378
23. Wang Y, Jia H-Z, Han K, Zhuo R-X, Zhang X-Z. Theranostic magnetic nanoparticles for efficient capture and in situ chemotherapy of circulating tumor cells. Journal of Materials Chemistry B 2013; 1 (27):3344.
24. Gleich B, Weizenecker J. Tomographic imaging using the nonlinear response of magnetic particles. Nature 2005, Jun 30; 435(7046):1214–7. https://doi.org/10.1038/nature03808 PMID: 15988521
25. Weizenecker J, Gleich B, Rahmer J, Dahnke H, Borgert J. Three-dimensional real-time in vivo magnetic particle imaging. Phys Med Biol 2009, Mar 7; 54(5):L1–L10. https://doi.org/10.1088/0031-9155/54/5/L01 PMID: 19204385
26. Haegele J, Rahmer J, Gleich B, Borgert J, Wojtczyk H, Panagiotopoulos N, et al. Magnetic particle imaging: Visualization of instruments for cardiovascular intervention. Radiology 2012; 265(3):933–8. https://doi.org/10.1148/radiol.12120424 PMID: 22996744
27. Vogel P, Lother S, Rückert MA, Kullmann WH, Jakob PM, Fidler F, Behr VC. MRI meets MPI: A bimodal MPI-MRI tomograph. IEEE Trans Med Imaging 2014, Oct; 33(10):1954–9. https://doi.org/10.1109/TMI.2014.2327515 PMID: 25291350
28. Franke J, Heinen U, Lehr H, Weber A, Jaspard F, Ruhm W, et al. System characterization of a highly integrated preclinical hybrid MPI-MRI scanner. IEEE Trans Med Imaging 2016, Mar 14.
29. Borgert J, Schmidt JD, Schmale I, Rahmer J, Bontus C, Gleich B, et al. Fundamentals and applications of magnetic particle imaging. J Cardiovasc Comput Tomogr 2012; 6(3):149–53. https://doi.org/10.1016/j.jcct.2012.04.007 PMID: 22682260
30. Saritas EU, Goodwill PW, Croft LR, Konkle JJ, Lu K, Zheng B, Conolly SM. Magnetic particle imaging (MPI) for NMR and MRI researchers. Journal of Magnetic Resonance 2012.
31. Duschka RL, Haegele J, Panagiotopoulos N, Wojtczyk H, Barkhausen J, Vogt FM, et al. Fundamentals and potential of magnetic particle imaging. Current Cardiovascular Imaging Reports 2013, Oct; 6 (5):390–8.

32. Shin TH, Choi Y, Kim S, Cheon J. Recent advances in magnetic nanoparticle-based multi-modal imaging. Chem Soc Rev 2015, Feb 5.

33. Kratz H, Eberbeck D, Wagner S, Taupitz M, Schnorr J. Synthetic routes to magnetic nanoparticles for MPI. Biomed Tech (Berl) 2013, Dec; 58(6):509–15.

34. Bulte JW, Walczak P, Janowski M, Krishnan KM, Arami H, Halkola A, et al. Quantitative "hot spot" imaging of transplanted stem cells using superparamagnetic tracers and magnetic particle imaging (MPI). Tomography 2015, Dec; 1(2):91–7. https://doi.org/10.18383/j.tom.2015.00172 PMID: 26740972

35. Zheng B, Vazin T, Goodwill PW, Conway A, Verma A, Saritas EU, et al. Magnetic particle imaging tracks the long-term fate of in vivo neural cell implants with high image contrast. Sci Rep 2015, Sep 11; 5:14055. https://doi.org/10.1038/srep14055 PMID: 26358296

36. Zheng B, von See MP, Yu E, Gunel B, Lu K, Vazin T, et al. Quantitative magnetic particle imaging monitors the transplantation, biodistribution, and clearance of stem cells in vivo. Theranostics 2016; 6 (3):291–301. https://doi.org/10.7150/thno.13728 PMID: 26909106

37. Lawaczeck R, Bauer H, Frenzel T, Hasegawa M, Ito Y, Kito K, et al. Magnetic iron oxide particles coated with carboxydextran for parenteral administration and liver contrasting. Pre-clinical profile of SH U555A. Acta Radiol 1997, Jul; 38(4 Pt 1):584–97. PMID: 9240682

38. Eberbeck D, Wiekhorst F, Wagner S, Trahms L. How the size distribution of magnetic nanoparticles determines their magnetic particle imaging performance. Applied Physics Letters 2011; 98 (18):182502.

39. Ferguson RM, Minard KR, Krishnan KM. Optimization of nanoparticle core size for magnetic particle imaging. J Magn Magn Mater 2009; 321(10):1548–51. https://doi.org/10.1016/j.jmmm.2009.02.083 PMID: 19606261

40. Ferguson RM, Khandhar AP, Kemp SJ, Arami H, Saritas EU, Croft LR, et al. Magnetic particle imaging with tailored iron oxide nanoparticle tracers. IEEE Trans Med Imaging 2015, May; 34(5):1077–84. https://doi.org/10.1109/TMI.2014.2375065 PMID: 25438306

41. Eberbeck D, Dennis CL, Huls NF, Krycka KL, Gruttner C, Westphal F. Multicore magnetic nanoparticles for magnetic particle imaging. Magnetics, IEEE Transactions on 2013; 49(1):269–74.

42. Starmans LW, Burdinski D, Haex NP, Moonen RP, Strijkers GJ, Nicolay K, Grüll H. Iron oxide nanoparticle-micelles (ion-micelles) for sensitive (molecular) magnetic particle imaging and magnetic resonance imaging. PLoS One 2013; 8(2):e57335. https://doi.org/10.1371/journal.pone.0057335 PMID: 23437371

43. Kemp SJ, Ferguson RM, Khandhar AP, Krishnan KM. Monodisperse magnetite nanoparticles with nearly ideal saturation magnetization. RSC Adv 2016; 6(81):77452–64.

44. Khandhar AP, Keselman P, Kemp SJ, Ferguson RM, Goodwill PW, Conolly SM, Krishnan KM. Evaluation of peg-coated iron oxide nanoparticles as blood pool tracers for preclinical magnetic particle imaging. Nanoscale 2017, Jan 19; 9(3):1299–306. https://doi.org/10.1039/c6nr08468k PMID: 28059427

45. Laurent S, Forge D, Port M, Roch A, Robic C, Vander Elst L, Muller RN. Magnetic iron oxide nanoparticles: Synthesis, stabilization, vectorization, physicochemical characterizations, and biological applications. Chemical Reviews 2008; 108(6):2064–110. https://doi.org/10.1021/cr068445e PMID: 18543879

46. Park J, An K, Hwang Y, Park JG, Noh HJ, Kim JY, et al. Ultra-large-scale syntheses of monodisperse nanocrystals. Nat Mater 2004, Dec; 3(12):891–5. https://doi.org/10.1038/nmat1251 PMID: 15568032

47. Palchoudhury S, An W, Xu Y, Qin Y, Zhang Z, Chopra N, et al. Synthesis and growth mechanism of iron oxide nanowhiskers. Nano Lett 2011; 11(3):1141–6. https://doi.org/10.1021/nl200136j PMID: 21309553

48. Landry R, Jacobs PM, Davis R, Shenouda M, Bolton WK. Pharmacokinetic study of ferumoxytol: A new iron replacement therapy in normal subjects and hemodialysis patients. Am J Nephrol 2005; 25 (4):400–10. https://doi.org/10.1159/000087212 PMID: 16088081

49. Na HB, Song IC, Hyeon T. Inorganic nanoparticles for MRI contrast agents. Advanced Materials 2009, Jun 5; 21(21):2133–48.

50. Sun S, Zeng H, Robinson DB, Raoux S, Rice PM, Wang SX, Li G. Monodisperse mfe2o4 (M = fe, co, mn) nanoparticles. J Am Chem Soc 2004, Jan 14; 126(1):273–9. https://doi.org/10.1021/ja0380852 PMID: 14709092

51. Tao K, Dou H, Sun K. Facile interfacial coprecipitation to fabricate hydrophilic amine-capped magnetite nanoparticles. Chemistry of Materials 2006; 18(22):5273–8.

52. Wang J, Yao M, Xu G, Cui P, Zhao J. Synthesis of monodisperse nanocrystals of high crystallinity magnetite through solvothermal process. Materials Chemistry and Physics 2009, Jan; 113(1):6–9.

53. Ravikumar C, Bandyopadhyaya R. Mechanistic study on magnetite nanoparticle formation by thermal decomposition and coprecipitation routes. The Journal of Physical Chemistry C 2011; 115(5):1380–7.

54. Simon GH, von Vopelius-Feldt J, Fu Y, Schlegel J, Pinotek G, Wendland MF, et al. Ultrasmall supraparamagnetic iron oxide-enhanced magnetic resonance imaging of antigen-induced arthritis: A comparative study between SHU 555 C, ferumoxtran-10, and ferumoxytol. Invest Radiol 2006, Jan; 41 (1):45–51. PMID: 16355039

55. Cornell RM, Schwertmann U. The iron oxides: Structure, properties, reactions, occurrences and uses. Wiley. com; 2003.

56. Jolivet J-P, Chanéac C, Tronc E. Iron oxide chemistry. From molecular clusters to extended solid networks. Chemical Communications 2004(5):481. https://doi.org/10.1039/b304532n PMID: 14973569

57. Guilbaud R, White ML, Poulton SW. Surface charge and growth of sulphate and carbonate green rust in aqueous media. Geochimica Et Cosmochimica Acta 2013; 108:141–53.

58. Génin J-MR, Refait P, Bourrié G, Abdelmoula M, Trolard F. Structure and stability of the fe (II)—fe (III) green rust fougerite mineral and its potential for reducing pollutants in soil solutions. Applied Geochemistry 2001; 16(5):559–70.

59. Mann S, Sparks NH, Couling SB, Larcombe MC, Frankel RB. Crystallochemical characterization of magnetic spinels prepared from aqueous solution. Journal of the Chemical Society, Faraday Transactions 1: Physical Chemistry in Condensed Phases 1989; 85(9):3033–44.

60. Garcell L, Morales MP, Andres-Verges M, Tartaj P, Serna CJ. Interfacial and rheological characteristics of maghemite aqueous suspensions. Journal of Colloid and Interface Science 1998; 205(2):470–5. https://doi.org/10.1006/jcis.1998.5654 PMID: 9735211

61. Lee EJ, Ribeiro C, Longo E, Leite ER. Oriented attachment: An effective mechanism in the formation of anisotropic nanocrystals. The Journal of Physical Chemistry B 2005; 109(44):20842–6. https://doi.org/10.1021/jp0532115 PMID: 16853702

62. Zhang ZJ, Wang ZL, Chakoumakos BC, Yin JS. Temperature dependence of cation distribution and oxidation state in magnetic mn-fe ferrite nanocrystals. Journal of the American Chemical Society 1998; 120(8):1800–4.

63. Mathew DS, Juang R-S. An overview of the structure and magnetism of spinel ferrite nanoparticles and their synthesis in microemulsions. Chemical Engineering Journal 2007, May; 129(1–3):51–65.

64. Gustafsson S, Fornara A, Petersson K, Johansson C, Muhammed M, Olsson E. Evolution of structural and magnetic properties of magnetite nanoparticles for biomedical applications. Crystal Growth & Design 2010, May 5; 10(5):2278–84.

65. Hyeon T, Lee SS, Park J, Chung Y, Na HB. Synthesis of highly crystalline and monodisperse maghemite nanocrystallites without a size-selection process. Journal of the American Chemical Society 2001; 123(51):12798–801. PMID: 11749537

66. Roca AG, Marco JF, Morales MDP, Serna CJ. Effect of nature and particle size on properties of uniform magnetite and maghemite nanoparticles. The Journal of Physical Chemistry C 2007; 111 (50):18577–84.

67. Giddings JC. Field-Flow fractionation. Separation Science and Technology 1984, Sep; 19(11–12):831–47.

68. Rogers HB, Anani T, Choi YS, Beyers RJ, David AE. Exploiting size-dependent drag and magnetic forces for size-specific separation of magnetic nanoparticles. Int J Mol Sci 2015, Aug 21; 16(8):20001–19. https://doi.org/10.3390/ijms160820001 PMID: 26307980

69. Jang J-T, Nah H, Lee J-H, Moon SH, Kim MG, Cheon J. Critical enhancements of MRI contrast and hyperthermic effects by dopant-controlled magnetic nanoparticles. Angewandte Chemie 2009; 121 (7):1260–4.

70. Tong S, Hou S, Zheng Z, Zhou J, Bao G. Coating optimization of superparamagnetic iron oxide nanoparticles for high T2 relaxivity. Nano Lett 2010, Nov 10; 10(11):4607–13. https://doi.org/10.1021/nl102623x PMID: 20939602

71. Ferguson RM, Minard KR, Khandhar AP, Krishnan KM. Optimizing magnetite nanoparticles for mass sensitivity in magnetic particle imaging. Med Phys 2011, Mar; 38(3):1619–26. https://doi.org/10.1118/1.3554646 PMID: 21520874

72. Schmidt-Kaler T. Landolt-Börnstein: Numerical data and functional relationships in science and technology, ed. Schaifers K. & Voigt H. Berlin: Springer), VI/2b; 1982.

73. Ahrens TJ. Rock physics & phase relations: A handbook of physical constants. American Geophysical Union; 1995.

74. Ge J, Hu Y, Biasini M, Beyermann WP, Yin Y. Superparamagnetic magnetite colloidal nanocrystal clusters. Angew Chem Int Ed Engl 2007; 46(23):4342–5. https://doi.org/10.1002/anie.200700197 PMID: 17465432

75. Lu C, Wang H, Ma J, Yuan H, Liang H, Wu L, et al. Facile synthesis of superparamagnetic magnetite nanoflowers and their applications in cellular imaging. RSC Adv 2016; 6(48):42649–55.

76. Thomas G, Demoisson F, Chassagnon R, Popova E, Millot N. One-step continuous synthesis of functionalized magnetite nanoflowers. Nanotechnology 2016, Apr 1; 27(13):135604. https://doi.org/10.1088/0957-4484/27/13/135604 PMID: 26900748

77. Kaiser R, Miskolczy G. Magnetic properties of stable dispersions of subdomain magnetite particles. J Appl Phys 1970, May 1; 41(3):1064–72.

78. Chantrell RW, Popplewell J, Charles S. Measurements of particle size distribution parameters in ferrofluids. Magnetics, IEEE Transactions on 1978; 14(5):975–7.

79. O'Grady K, Bradbury A, Popplewell J, Charles SW, Chantrell RW. The effect of field induced texture on the properties of a fine particle system. J Magn Magn Mater 1985; 49(1):106–16.

80. Embs J, Muler HW, Krill CE III, Meyer F, Natter H, Muler B, et al. Particle size analysis of ferrofluids. Magnetohydrodynamics 2001; 37:222–9.

81. Millan A, Urtizberea A, Silva NJO, Palacio F, Amaral VS, Snoeck E, Serin V. Surface effects in maghemite nanoparticles. J Magn Magn Mater 2007; 312(1):L5–9.

82. Paulus PM, Bönnemann H, Van der Kraan AM, Luis F, Sinzig J, De Jongh LJ. Magnetic properties of nanosized transition metal colloids: The influence of noble metal coating. The European Physical Journal D-Atomic, Molecular, Optical and Plasma Physics 1999; 9(1):501–4.

83. van Leeuwen DA, van Ruitenbeek JM, de Jongh LJ, Ceriotti A, Pacchioni G, Häberlen OD, Rösch N. Quenching of magnetic moments by ligand-metal interactions in nanosized magnetic metal clusters. Phys Rev Lett 1994, Sep 5; 73(10):1432–5. https://doi.org/10.1103/PhysRevLett.73.1432 PMID: 10056791

84. Wiedenmann A. Small-angle neutron scattering investigations of magnetic nanostructures using polarized neutrons. Journal of Applied Crystallography 2000; 33(3):428–32.

85. Anthore R, Petipas C, Chandesris D, Martinet A. X-ray and magnetization studies of the geometrical parameters of the grains of a ferrofluid. Le Journal De Physique Colloques 1977; 38(C2):C2–203.

86. Hrianca I, Caizer C, Schlett Z. Dynamic magnetic behavior of fe3o4 colloidal nanoparticles. J Appl Phys 2002; 92(4):2125–32.

87. Salabas EL, Rumplecker A, Kleitz F, Radu F, Schüth F. Exchange anisotropy in nanocasted co3o4 nanowires. Nano Lett 2006; 6(12):2977–81. https://doi.org/10.1021/nl060528n PMID: 17163743

88. Biederer S, Knopp T, Sattel F, Lüdtke-Buzug K, Gleich B, Weizenecker J, et al. Magnetization response spectroscopy of superparamagnetic nanoparticles for magnetic particle imaging. Journal of Physics D: Applied Physics 2009, Oct 21; 42(20):205007.

89. Kaul M, Weber O, Heinen U, Reitmeier A, Mummert T, Jung C, et al. Combined preclinical magnetic particle imaging and magnetic resonance imaging: Initial results in mice. RöFo—Fortschritte Auf Dem Gebiet Der Röntgenstrahlen Und Der Bildgebenden Verfahren 2015, Apr 21; 187(05):347–52.

90. Dieckhoff J, Kaul MG, Mummert T, Jung C, Salamon J, Adam G, et al. In vivo liver visualizations with magnetic particle imaging based on the calibration measurement approach. Phys Med Biol 2017, May 7; 62(9):3470–82. https://doi.org/10.1088/1361-6560/aa562d PMID: 28035904

91. Lawaczeck R, Menzel M, Pietsch H. Superparamagnetic iron oxide particles: Contrast media for magnetic resonance imaging. Applied Organometallic Chemistry 2004; 18(10):506–13.

92. Arbab AS, Yocum GT, Kalish H, Jordan EK, Anderson SA, Khakoo AY, et al. Efficient magnetic cell labeling with protamine sulfate complexed to ferumoxides for cellular MRI. Blood 2004, Aug 15; 104(4):1217–23. https://doi.org/10.1182/blood-2004-02-0655 PMID: 15100158

93. Kalish H, Arbab AS, Miller BR, Lewis BK, Zywicke HA, Bulte JW, et al. Combination of transfection agents and magnetic resonance contrast agents for cellular imaging: Relationship between relaxivities, electrostatic forces, and chemical composition. Magn Reson Med 2003, Aug; 50(2):275–82. https://doi.org/10.1002/mrm.10556 PMID: 12876703

94. Mailänder V, Lorenz MR, Holzapfel V, Musyanovych A, Fuchs K, Wiesneth M, et al. Carboxylated superparamagnetic iron oxide particles label cells intracellularly without transfection agents. Mol Imaging Biol 2008; 10(3):138–46. https://doi.org/10.1007/s11307-007-0130-3 PMID: 18297365

95. Frank JA, Miller BR, Arbab AS, Zywicke HA, Jordan EK, Lewis BK, et al. Clinically applicable labeling of mammalian and stem cells by combining superparamagnetic iron oxides and transfection agents. Radiology 2003, Aug; 228(2):480–7. https://doi.org/10.1148/radiol.2281020638 PMID: 12819345

96. Arbab AS, Yocum GT, Wilson LB, Parwana A, Jordan EK, Kalish H, Frank JA. Comparison of transfection agents in forming complexes with ferumoxides, cell labeling efficiency, and cellular viability. Molecular Imaging 2004; 3(1):24–32. https://doi.org/10.1162/153535004773861697 PMID: 15142409

97. Treuel L, Jiang X, Nienhaus GU. New views on cellular uptake and trafficking of manufactured nanoparticles. J R Soc Interface 2013, May 6; 10(82):20120939. https://doi.org/10.1098/rsif.2012.0939 PMID: 23427093

98. Ocampo SM, Rodriguez V, de la Cueva L, Salas G, Carrascosa JL, Rodríguez MJ, et al. G-force induced giant efficiency of nanoparticles internalization into living cells. Sci Rep 2015, Oct 19; 5:15160. https://doi.org/10.1038/srep15160 PMID: 26477718

99. Weissleder R, Nahrendorf M, Pittet MJ. Imaging macrophages with nanoparticles. Nature Materials 2014; 13(2):125–38. https://doi.org/10.1038/nmat3780 PMID: 24452356

100. Kaul MG, Mummert T, Jung C, Salamon J, Khandhar AP, Ferguson RM, et al. In vitro and in vivo comparison of a tailored magnetic particle imaging blood pool tracer with resovist. Phys Med Biol 2017, May 7; 62(9):3454–69. https://doi.org/10.1088/1361-6560/aa5780 PMID: 28060771

101. Scharlach C, Müller L, Wagner S, Kobayashi Y, Kratz H, Ebert M, et al. LA-ICP-MS allows quantitative microscopy of europium-doped iron oxide nanoparticles and is a possible alternative to ambiguous prussian blue iron staining. Journal of Biomedical Nanotechnology 2016; 12(5):1001–10. PMID: 27305821

102. Kim JA, Åberg C, Salvati A, Dawson KA. Role of cell cycle on the cellular uptake and dilution of nanoparticles in a cell population. Nat Nanotechnol 2011, Nov 6; 7(1):62–8. https://doi.org/10.1038/nnano.2011.191 PMID: 22056728

103. Fortune B, Mellon G. Determination of iron with o-phenanthroline: A spectrophotometric study. Industrial & Engineering Chemistry Analytical Edition 1938, Feb; 10(2):60–4.

104. Braunschweig J, Bosch J, Heister K, Kuebeck C, Meckenstock RU. Reevaluation of colorimetric iron determination methods commonly used in geomicrobiology. J Microbiol Methods 2012, Apr; 89(1):41–8. https://doi.org/10.1016/j.mimet.2012.01.021 PMID: 22349079

105. Crabbe A, Vandeputte C, Dresselaers T, Sacido AA, Verdugo JM, Eyckmans J, et al. Effects of MRI contrast agents on the stem cell phenotype. Cell Transplant 2010; 19(8):919–36. https://doi.org/10.3727/096368910X494623 PMID: 20350351

106. Wells J, Paysen H, Kosch O, Loewa N, Schmitzberger F, Makowski M, et al. Characterizing a preclinical magnetic particle imaging system with separate pick-up coil. IEEE Transactions on Magnetics 2017.

107. Hansen PC. Discrete inverse problems: Insight and algorithms (philadelphia, PA: SIAM). 2010.